

Analysing the Microstructures and Pin-on-Disc Wear Properties of 1010 Steel-Based and B₄C-Added Materials Produced through Powder Metallurgy

Mehtap Demirel, Vahdettin Koç

Vocational School of Technical Sciences, Adiyaman University, Adiyaman, Turkey

Email: demirel_mehtap@yahoo.com

How to cite this paper: Demirel, M. and Koç, V. (2021) Analysing the Microstructures and Pin-on-Disc Wear Properties of 1010 Steel-Based and B₄C-Added Materials Produced through Powder Metallurgy. *World Journal of Engineering and Technology*, 9, 682-707.

<https://doi.org/10.4236/wjet.2021.93047>

Received: June 23, 2021

Accepted: August 28, 2021

Published: August 31, 2021

Copyright © 2021 by author(s) and Scientific Research Publishing Inc. This work is licensed under the Creative Commons Attribution International License (CC BY 4.0).

<http://creativecommons.org/licenses/by/4.0/>



Open Access

Abstract

The present study makes use of two distinct production methods. The first method involves producing 1010 steel-based materials containing SiC, MgO, H₃BO₃, and B₄C (wt%10 - wt%30) with varying weights through powder metallurgy. This step was followed by hot pressing. In the second group, after all the chemicals were stirred, 20 ml of epoxy and epoxy hardener were added to the mixture. Then, the mixture was set aside to harden. XRD and SEM-EDS analyses were conducted on the mixture to observe the morphological impacts. Furthermore, friction coefficient values of the materials were also identified following wear tests under varying weights. The XRD analyses revealed the phase structures of Fe₃C, SiC, MgO, H₃BO₃, B₄C, and Fe₂O₃. As for the SEM-EDS analyses, they concluded the surface appearance of S60 and S55B20, the hot-pressed materials, dependent on liquid phase sintering. SEM of epoxy-based S60E20 and S55B20E20 revealed white spherical structures and a flat matrix structure with shallow surface holes. In the pin-on-disc wear experiment, the friction coefficient value was reduced with the addition of SiC, MgO, and H₃BO₃ (S60) to 1010 steel (S100). By adding various amounts of B₄C, the friction coefficient was reduced even further, resulting in the improvement of wear properties.

Keywords

1010 Steel, B₄C, Epoxy, Hot Pressing, Wear

1. Introduction

Many engineering components deteriorate due to degradation processes such as

fatigue, corrosion, and wear occurring on material surfaces [1] [2] [3]. Therefore, materials employed particularly in agricultural, mining, oil, and petrochemicals industries are improved by surface engineers, leading to the use of new products. Different types of steel and steel alloys available in the current market are appealing owing to their versatile microstructures, properties, and low costs [4] [5]. Thus, certain types of steel do not fulfil the safety requirements involving tear resistance [6]. The results in the production of novel materials contain steel.

Stainless steels produce satisfying results in applications requiring a sound balancing of costs, mechanical endurance, and corrosion resistance. However, depending on the environment and working conditions, stainless steels might display negative wear resistance in certain cases. Surface modification methods were developed to counter this issue [7] [8] [9] [10]. Coating methods are usually favoured to increase the wear resistance of materials. Laser coating, pulverisation, and welding are the methods employed for coating [7]. Methods involving welding are the most cost-efficient among other procedures [10]. Furthermore, coating iron-based materials with boron or boride powders have also proved to be effective in improving wear properties [11] [12]. Studies revealed that when compared with other coating methods such as carburisation and nitriding, boronising displays the best results in terms of wear properties [13] [14] [15]. Products combining such surface features are ideal for certain industrial applications requiring high tribological performance such as gear cases for turbines, camshafts, weapons, and parts of agricultural machines [16].

Steel is a particular alloy used in various industrial applications owing to its low costs, malleability, weldability, and thermal processability [17]. The use of reinforcing powders is commonplace in mechanical alloying and welding. SiC powder is often used to achieve desired surface properties in steel [17]. Li *et al.* [18] reported that liquid phase sintering is not a suitable method for adding SiC to the element iron due to the high reactivity of the silicon carbide and iron melt. On the other hand, sintering also takes a long time (2 hours) in case of the use of powder metallurgy for production, in which a heavy interface reaction occurs between iron and silicon carbide [17]. Wu *et al.* [19] examined the effects of 316L stainless steel reinforced with SiC using laser melting composition (LMC) and found that the addition of SiC improves the microstructure.

Generally speaking, these studies indicate that while steels with good properties are rendered inadequate with the advancement of technology, compounds containing boron bring about positive tribological effects on steel. However, the studies also reveal that boron or compounds containing boron are usually used by means of coating the surface of the steel and produce positive results. SiC was also found to improve the microstructural and surface features of steel. However, these positive results arose following a prolonged sintering process during production lasting 2 hours.

By involving adding and producing the B₄C compound to 1010 steel not through

coating but by means of powder metallurgy, the present study both assesses the impacts of B₄C and examines the effects of powder metallurgy on wear properties. Furthermore, in addition to B₄C in varying amounts, compounds like SiC, MgO, and H₃BO₃ were added to 1010 steel in order to observe their effects. Additionally, the 1010 steel, SiC, MgO, H₃BO₃, and B₄C mixed mechanically were added to equal amounts (20 ml) of epoxy + epoxy hardener to examine morphological effects and impacts on wear properties.

2. Experimental Procedure

2.1. Materials and Produce Process

The materials for which weight percentage (%) values are given in **Table 1** were produced within the scope of this study through powder metallurgy.

Two different groups were formed during production. In the first group, after the amounts of 1010 steel, SiC, MgO, H₃BO₃, and B₄C indicated in **Table 1** were mixed mechanically for an hour using a mixer, they were used as S100, S60, S60B10, S55B20, and S45B30. All the materials with diameters of 2 mm and heights of 2 mm during the hot pressing procedure were unidirectionally hot-pressed under a force of 45 MPa and a temperature of 950 °C. A pressure of 10 - 4 mbar was applied to the materials during hot pressing under vacuum conditions. Then, as shown in **Figure 1**, the temperature was increased to 950 °C in 10 minutes, the materials were left to rest under 45 MPa in 950 °C for 30 minutes before being cooled to room temperature in 5 minutes.

In the second group; to prepare the materials S60B10E20, S55B20E20, and S45B30E20, the amounts of 1010 steel and powdered compounds of SiC, MgO, H₃BO₃, and B₄C indicated in **Table 1** were, once again, mixed mechanically for an hour using a mixer before being added to a mixture containing 15 ml of epoxy and 5 ml of hardener and mixed again. Then, the mixture was poured into polymer moulds with diameters of 3 mm and heights of 2 mm before being placed

Table 1. Weight % values of materials produced by means of powder metallurgy.

Samples	1010 steel (%wt.)	SiC (%wt.)	MgO (%wt.)	H ₃ BO ₃ (%wt.)	B ₄ C (%wt.)	Epoxy + hardener (ml)
S100	100	-	-	-	-	-
S60	60	10	15	15	-	-
S60B10	60	5	10	15	10	-
S55B20	55	5	10	10	20	-
S45B30	45	5	10	10	30	-
S100E20	100	-	-	-	-	20
S60E20	60	10	15	15	-	20
S60B10E20	60	5	10	15	10	20
S55B20E20	55	5	10	10	20	20
S45B30E20	45	5	10	10	30	20

on a vibration device for 30 minutes to distribute the mixture in the moulds homogenously. Then, the moulds were set aside with no vibration to harden in room temperature.

2.2. Characterization

XRD and SEM-EDS devices were used to analyse the microstructures and chemical properties of the first group of materials produced through powder metallurgy as well as those of the mixture of 1010 steel, SiC, MgO, H₃BO₃, and B₄C added into epoxy and hardener. Pin-on-disc wear tests were conducted under varying weights to examine their wear resistances. While Bruker D8 Advance was used for XRD (X-Ray Diffractometer), SEM-EDS analysis was conducted by scanning electron microscope (SEM, JEOL JSM 7001 F) and electron dispersive spectroscopy (EDS, Oxford INCA).

Figure 2 shows a visual of the wear device used for the wear test conducted under different weights. Tribometer T10/20 was used as the wear device. Alumina (Al₂O₃) balls with diameters of 6 mm were used during pin-on-disc wear tests. Furthermore, the effects of differences in loads were examined by making use of varying wear loads of 10N, 20N, and 30N. A fixed shear rate of 300 rpm

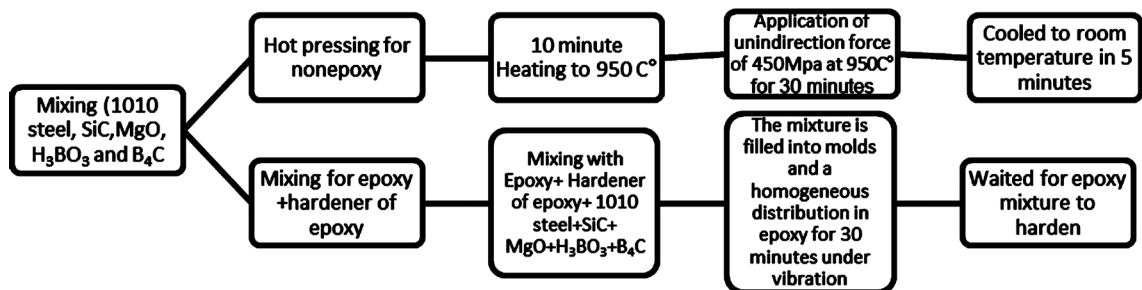


Figure 1. Hot pressing production stages.

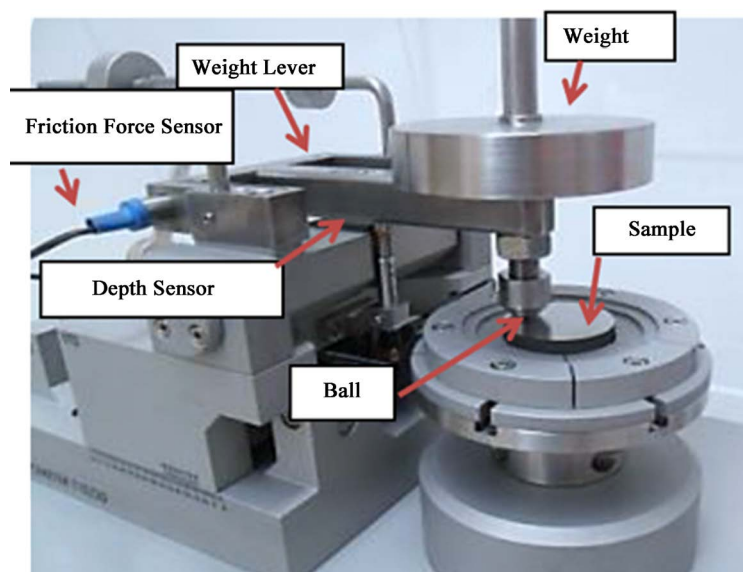


Figure 2. The wear test device used for the experiments.

and a fixed sliding distance of 300 m were applied during the wear test. Additionally, the interface temperatures during the wear process were measured using a TESTO 875-1i thermal camera. This thermal camera measures the temperatures in the wear contact points on the interface for every 50 m of sliding distance to observe the differences in temperature arising on the material during wear. Among the temperature graph values recorded with the thermal camera during wear, the maximum temperature values are the ones above the wearing line. The temperature graphs were considered separately for each load and the changes in temperature originating from friction were examined. Furthermore, the impacts of temperature on the friction coefficient of the material were identified. Thermal photographs taken during the friction process were examined and the visuals were then placed accordingly. During production, the effects of both the compound B_4C added in varying amounts and the mixture of 1010 steel and compounds SiC , MgO , H_3BO_3 , and B_4C added into the epoxy + hardener mixture were assessed.

3. Results

3.1. XRD

XRD analysis results for the material S100 the weight of which (wt) is 100% 1010 steel and the material S60 containing 1010 steel, SiC , MgO , and H_3BO_3 are shown in **Figure 3(a)** & **Figure 3(b)**. The XRD analysis conducted on S100 showed that the material contains Fe_3C (**Figure 3(a)**). As for **Figure 3(b)**, it shows that the material S60 has a chemical structure containing Fe_3C with a lower peak intensity along with SiC and H_3BO_3 .

Figures 4(a)-(c) shows the XRD analysis results for the materials S60B10, S55B20, and S45B30 produced by adding varying amounts (wt%10-30) of B_4C to the material S60. XRD analyses revealed that all the materials contain Fe_3C and steel in addition to the phase structures of SiC , MgO , H_3BO_3 , and B_4C . Furthermore, the materials S60B10, S55B20, and S45B30 also contain the phase structure Fe_2O_3 in addition to the phases listed above. The examination of XRD peak distributions for materials containing wt10-20% of B_4C revealed that while the

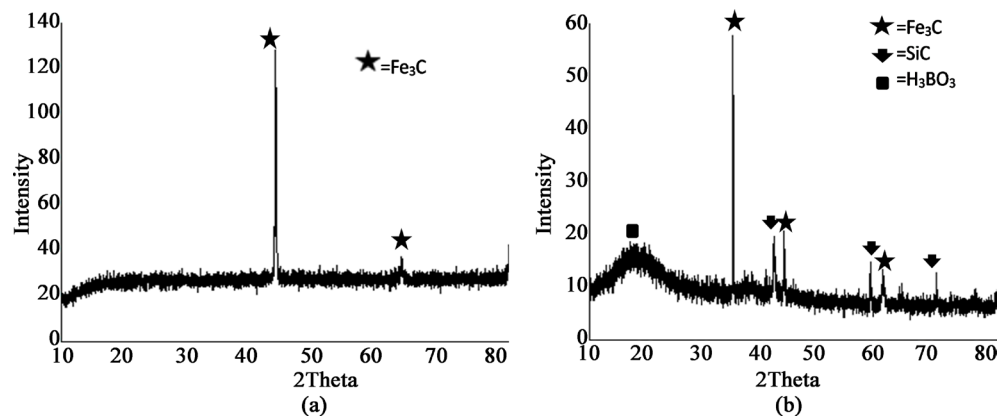


Figure 3. XRD graphs for the materials (a) S100 and (b) S60.

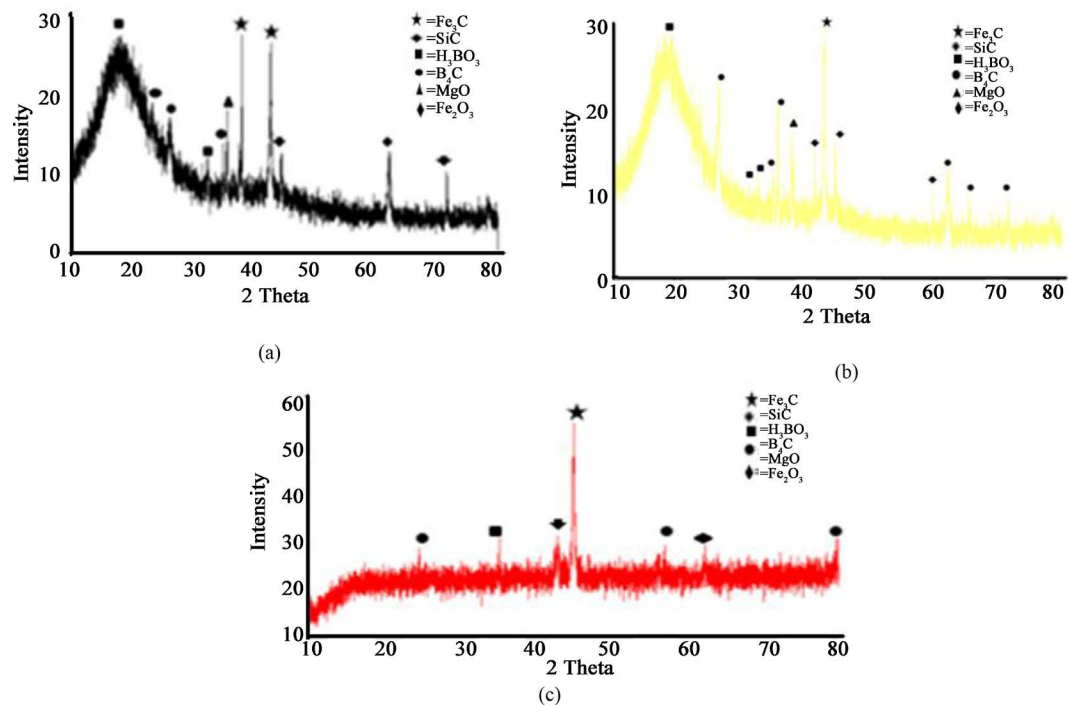


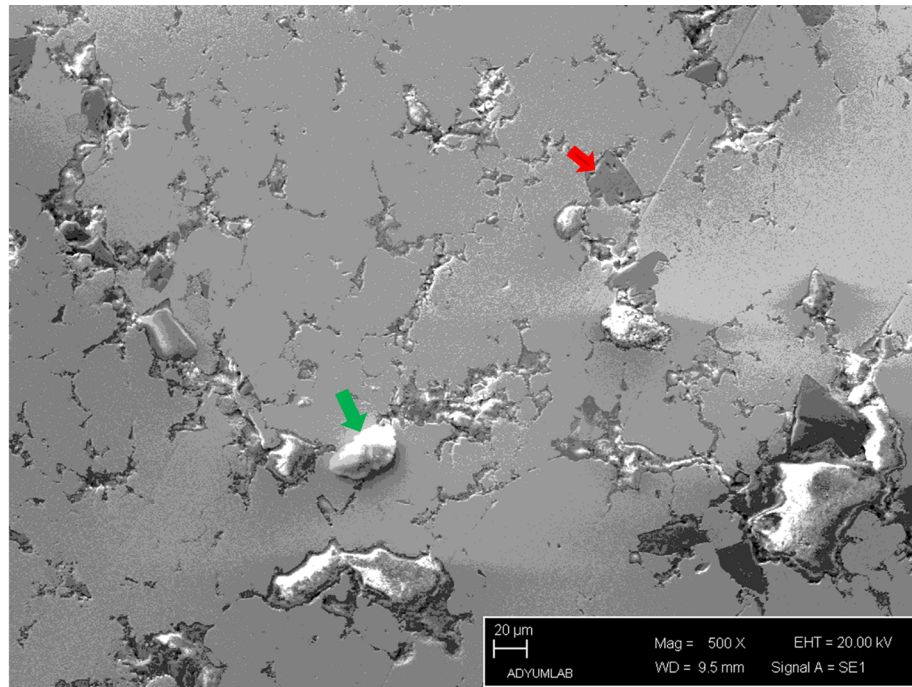
Figure 4. XRD results for the materials (a) S60B10; (b) S55B20; and (c) S45B30.

peaks are distributed clearly and distinctly for S60B10 and S55B20, the peak distribution rate declines for S45B30. However, the material S45B30 containing wt30% B_4C have lower peak distributions for reinforcement compounds and higher peak intensity as shown in **Figure 4(c)** displaying XRD analysis results.

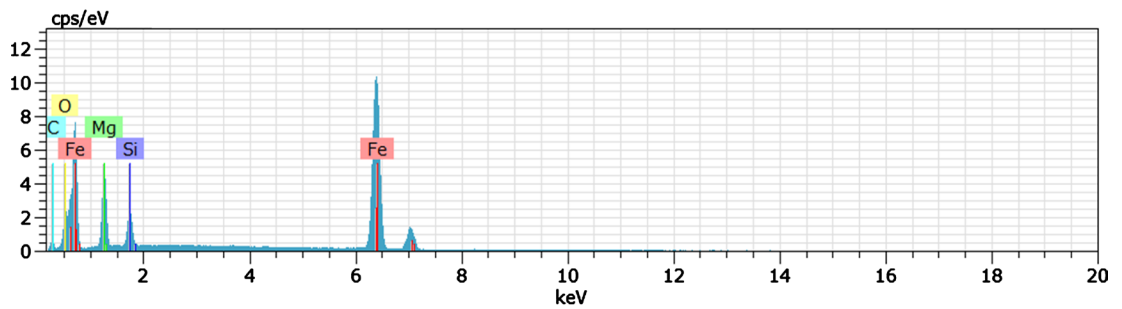
3.2. SEM-EDS

The SEM of S60 taken at 500X magnification is also given **Figure 5(a)**. EDS results from the surface of the S60 are also observed in **Figure 5(b)** & **Figure 5(c)**. It is observed that liquid phase sintering is generally occurring from S60, while it is also determined that 2 different phase structures exist outside the structure (**Figure 5(a)**). Two different structures, which occur outside the matrix structure, are irregularly distributed in the matrix and their shape and size appear different (**Figure 5(a)**). It is also observed that a phase structure occurs at different elevation (**Figure 5(a)**) (shown in **▶**). It is observed that the S60 material from the EDS result, which is generally acquired from the surface of the image, contains compounds containing Fe, Mg, Si, C and O content (**Figure 5(b)**) (shown in **▶**). It is also shown in **Figure 5(c)** & **Figure 5(d)**, where the SEM image contains Si and C-content compounds in its dark gray phase (from **▶** point) with Mg, C and O content from the point-of-point EDS result from the different height phase (from **▶** point) displayed in the image.

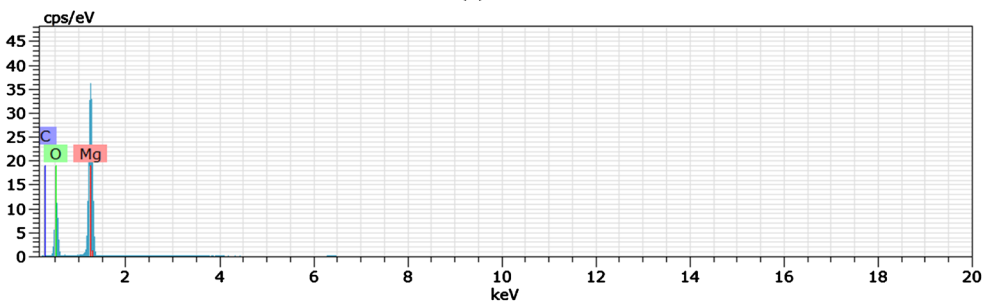
The SEM visual obtained after the material S55B20 containing wt20% B_4C was zoomed 500 times shows a structure with indefinite grain boundaries due to liquid phase sintering as the main phase (**Figure 6(a)**). Besides the main structure, the structures containing Mg, C, and O observed in the material S60 and



(a)



(b)



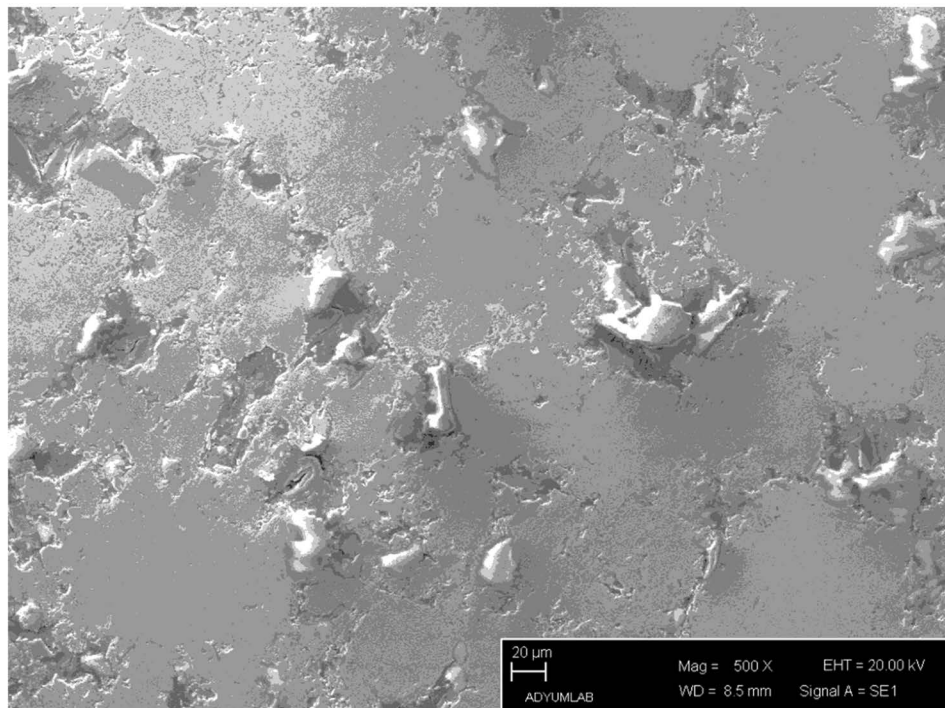
El AN Series un. C norm. C Atom. C Error (1 Sigma)
 [wt.%] [wt.%] [at.%] [wt.%]

Mg 12 K-series	35.34	50.30	39.35	1.96
O 8 K-series	32.09	45.68	54.28	3.85
C 6 K-series	2.82	4.02	6.36	0.71

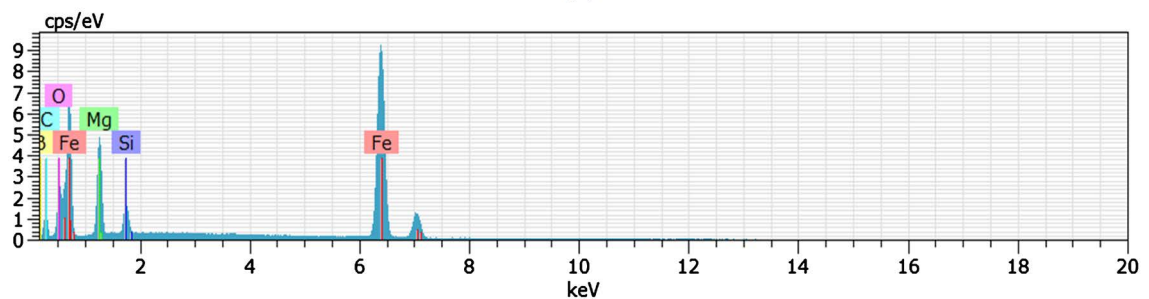
Total: 70.26 100.00 100.00

(c)

Figure 5. (a) SEM visual and (b) general EDS results for S60, point-based EDS analysis results taken from phases indicated as (c) and (d) .



(a)



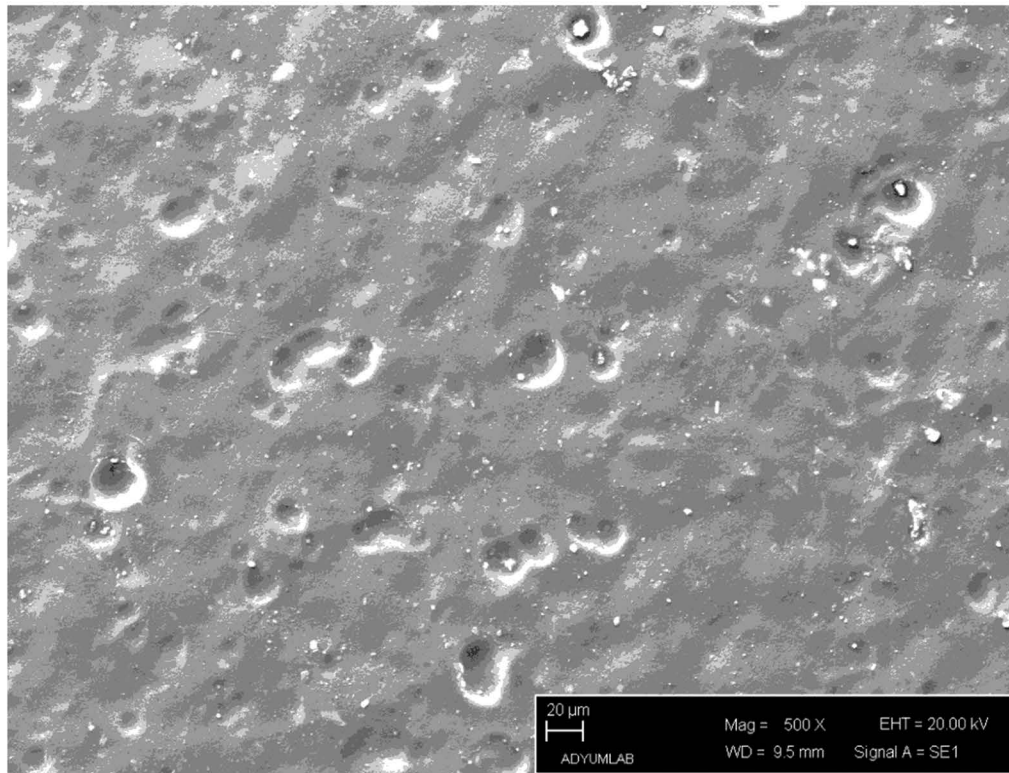
(b)

Figure 6. (a) The SEM visual and (b) general EDS analysis results for S55B20.

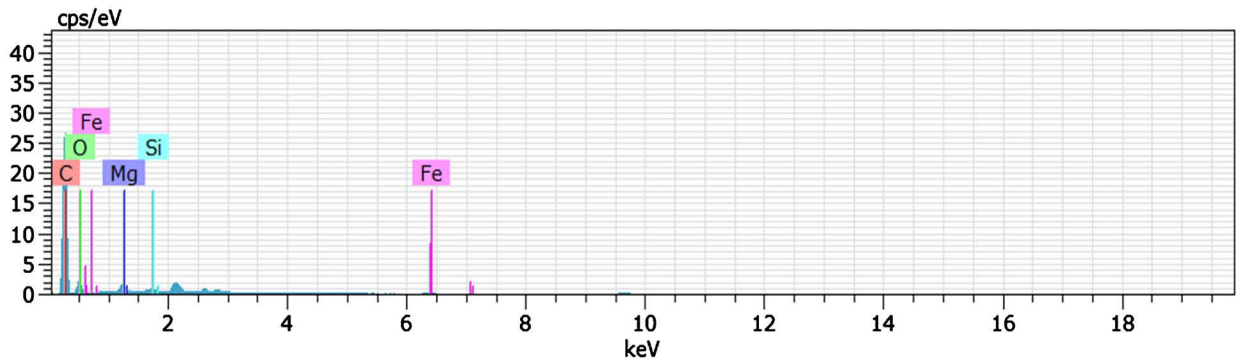
compounds containing Si and C are also present in S55B20 (**Figure 6(a)**). The general EDS results for the material S55B20 shown in **Figure 3(b)** indicates that the material is made of structures containing the elements Fe, C, Si, Mg, and O.

The SEM visual of the material S60E20 produced by adding a 1010 steel mixture into 15 ml of epoxy and 5 ml of hardener zoomed 500 times revealed a flat surface with surface holes and different, small, and white structures on the surface (**Figure 7(a)**). The general EDS result obtained from the surface shows that the material consists of phases containing Fe, Si, Mg, C, and O (**Figure 7(b)**) with the white structures on the surface containing Fe, Si, C, and O according to the point-based EDS analysis (**Figure 7(c)**).

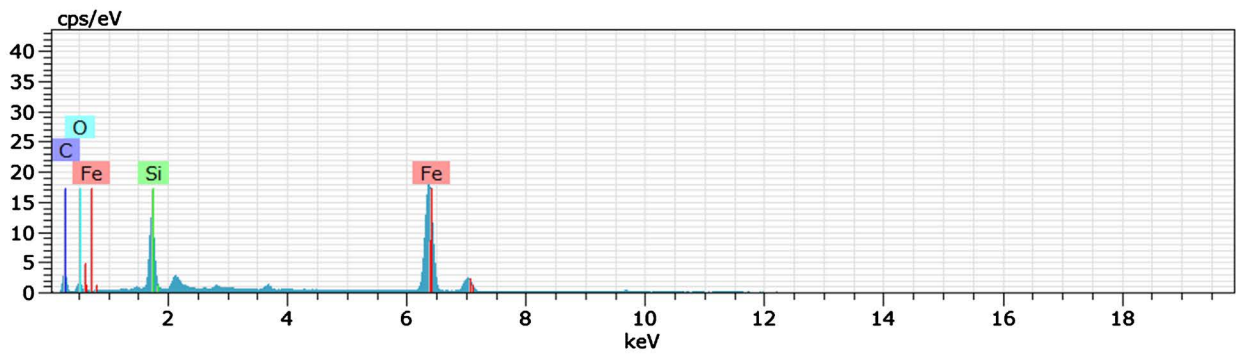
The SEM visual for the material S55B20E20 with wt55% 1010 steel and wt20% B₄C along with 20 ml of epoxy + hardener zoomed 500 times and the general EDS analysis result for the surface are given in **Figure 8(a)** & **Figure 8(b)**. The SEM visual revealed that the main structure of S55B20E20 is flat, similarly to



(a)

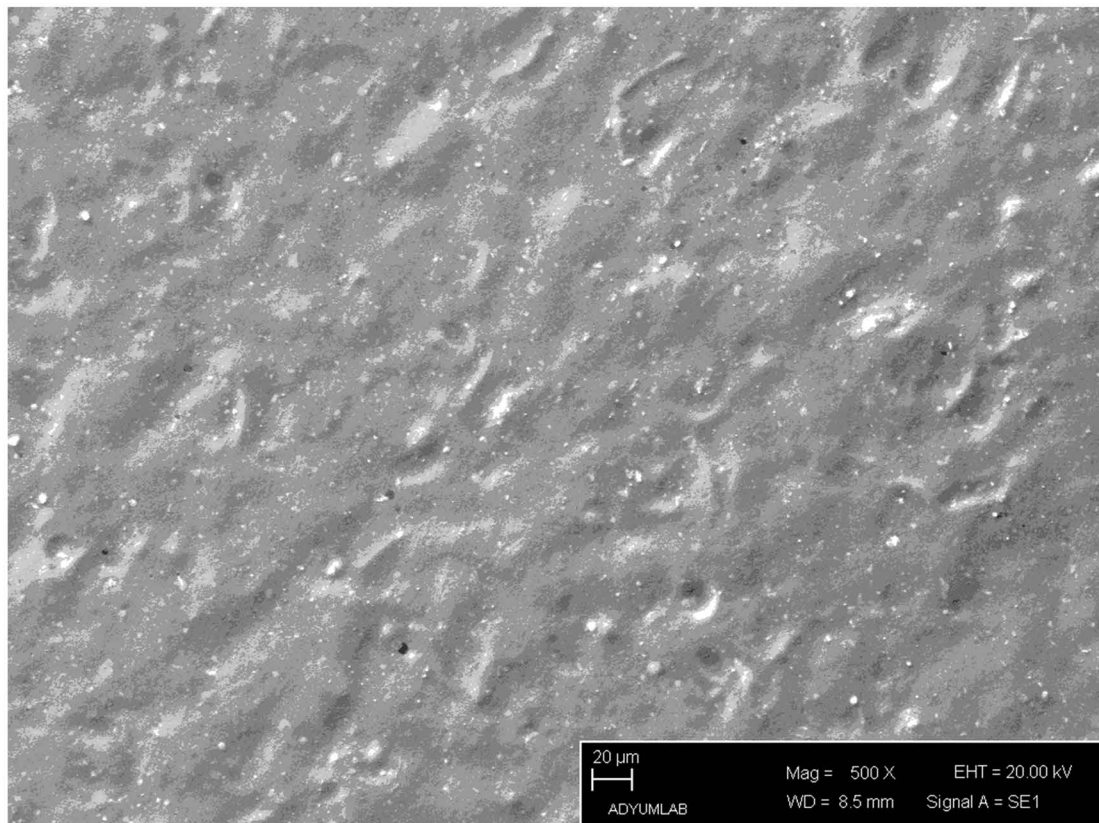


(b)

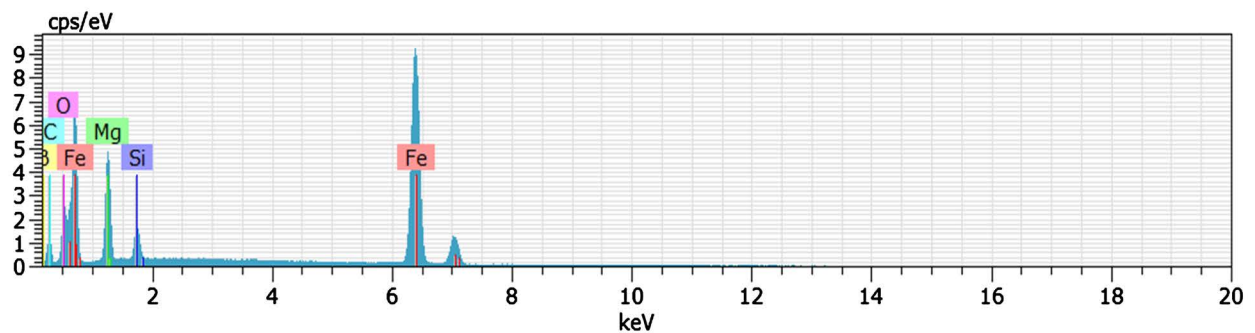


(c)

Figure 7. (a) SEM results, (b) general EDS results from the surface, and (c) EDS results taken from the point for S60E20.



(a)



(b)

Figure 8. (a) SEM and (b) general EDS analysis results obtained from the surface for the material S55B20E20.

S60E20, with fewer surface holes and white, homogeneously-distributed, small structures like S60E20 (**Figure 8(a)**). Furthermore, when compared with S60E20, white spherical structures are smaller in size and greater in quantity on the surface of S55B20E20 (**Figure 7(a)**, **Figure 8(a)**). The general EDS analysis for the surface shows that S55B20E20 consists of structures containing the elements Fe, Si, Mg, B, C, and O.

3.3. Figures and Tables

Figure 9 shows the friction coefficient-sliding distance curves (a) for the 1010

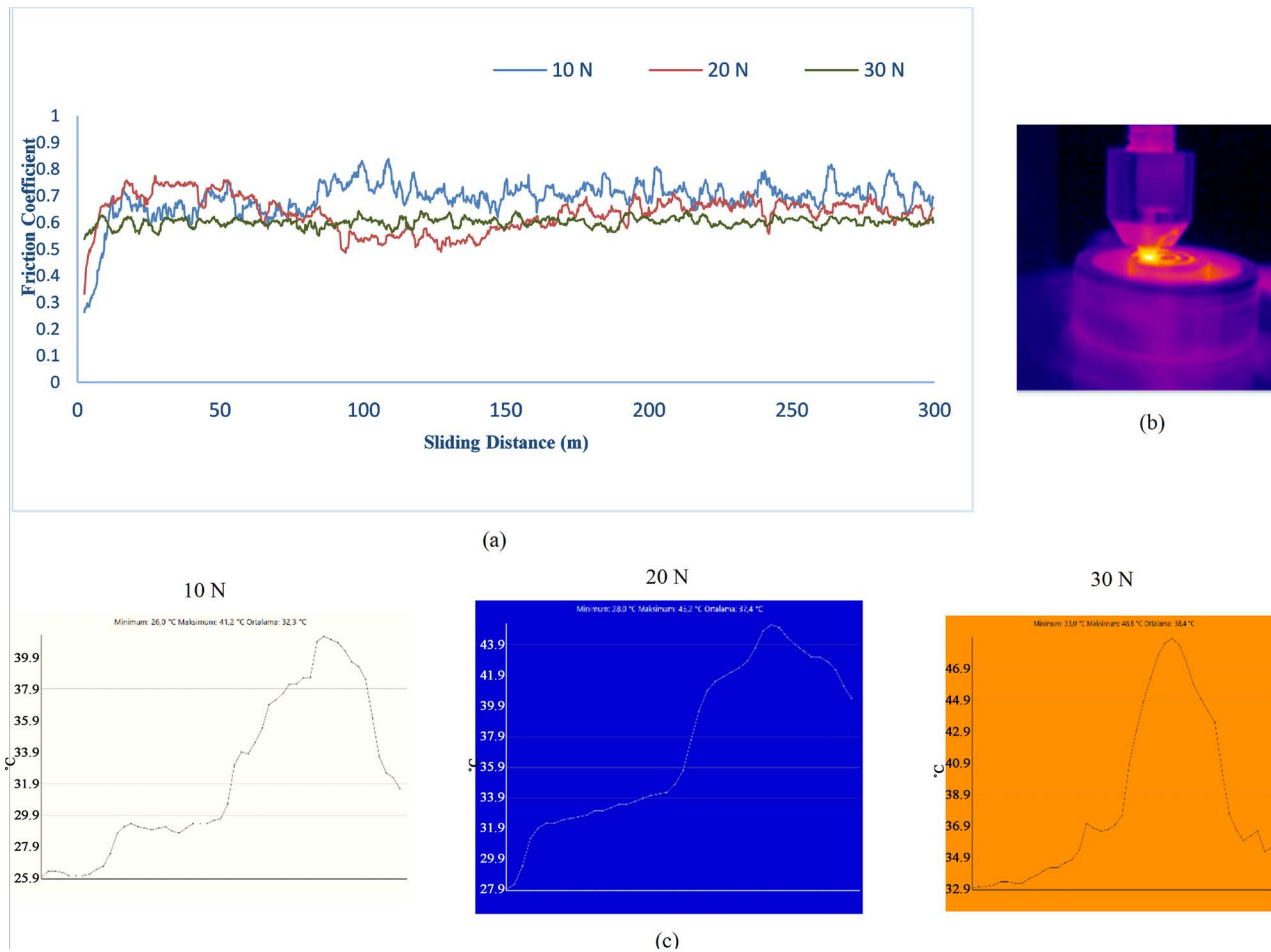


Figure 9. (a) The graph of friction coefficient-sliding distance between 10N - 30N; (b) The thermal visual taken with the thermal camera from the surface during the wear test; (c) the graph showing differences in surface temperature between 10N - 30N for the material S100.

steel with no additions (S100) for loads varying between 10N and 30N as well as the thermal visual of the surface captured with the thermal camera during the wear test conducted under a load of 30N. Furthermore, **Figure 9(c)** shows temperature measurements recorded with the thermal camera for every 50 m of sliding distance for varying loads (10N - 30N) as well as the graph indicating the changes in temperature on the surface at the end of 300 m. The friction coefficient-sliding distance graph reveals that for all the loads, S100 displays fluctuating friction peaks and similar inclinations (**Figure 9(a)**). One can see from **Figure 9(a)** that the first stage of the friction and wear tests conducted under loads varying between 10N and 30N is unstable with the friction coefficient constantly increasing with significant fluctuations. After the first stage, the friction peaks were found to be more stable; however, under all the loads, the friction peaks were fluctuating (**Figure 9(a)**). For S100, the friction coefficient values dropped visibly, particularly after the sliding distance of 100 m as the load increased. Furthermore, **Figure 9(c)** shows the rapid increase in the surface temperature for S100 under all the loads, particularly after the sliding distance of 100 m.

Figure 10(a) shows the results of the pin-on-disc wear test conducted on the 1010 steel-based S60 containing SiC, MgO, and H₃BO₃. Similar, fluctuating friction peaks in the friction coefficient-sliding distance curves of S60 for all the loads in the experiment are also visible in this figure. The peaks in the first stage of the wear test conducted on S60 under all the weight were unstable; the friction coefficient increased constantly with significant fluctuations during this stage (**Figure 10(a)**). Furthermore, **Figure 10(a)** also shows that the friction of coefficient values increase as the load increases. At the end of the sliding distance of 300m, it was clear that the highest friction coefficient was around 0.6 during the wear test conducted under the load of 30N (**Figure 10(a)**). **Figure 10(c)** shows that at the end of the temperature measurements made at regular intervals for 300 m under the loads varying between 10N and 30N, the temperature rose rapidly until a certain sliding distance but after 150 m of sliding distance, it decreases at the same speed.

Figures 11(a)-(c) shows the friction coefficient-sliding distance graph obtained at the end of the pin-on-disc wear test under loads varying between 10N and 30N for the material containing wt10% B₄C. The analysis revealed that at the

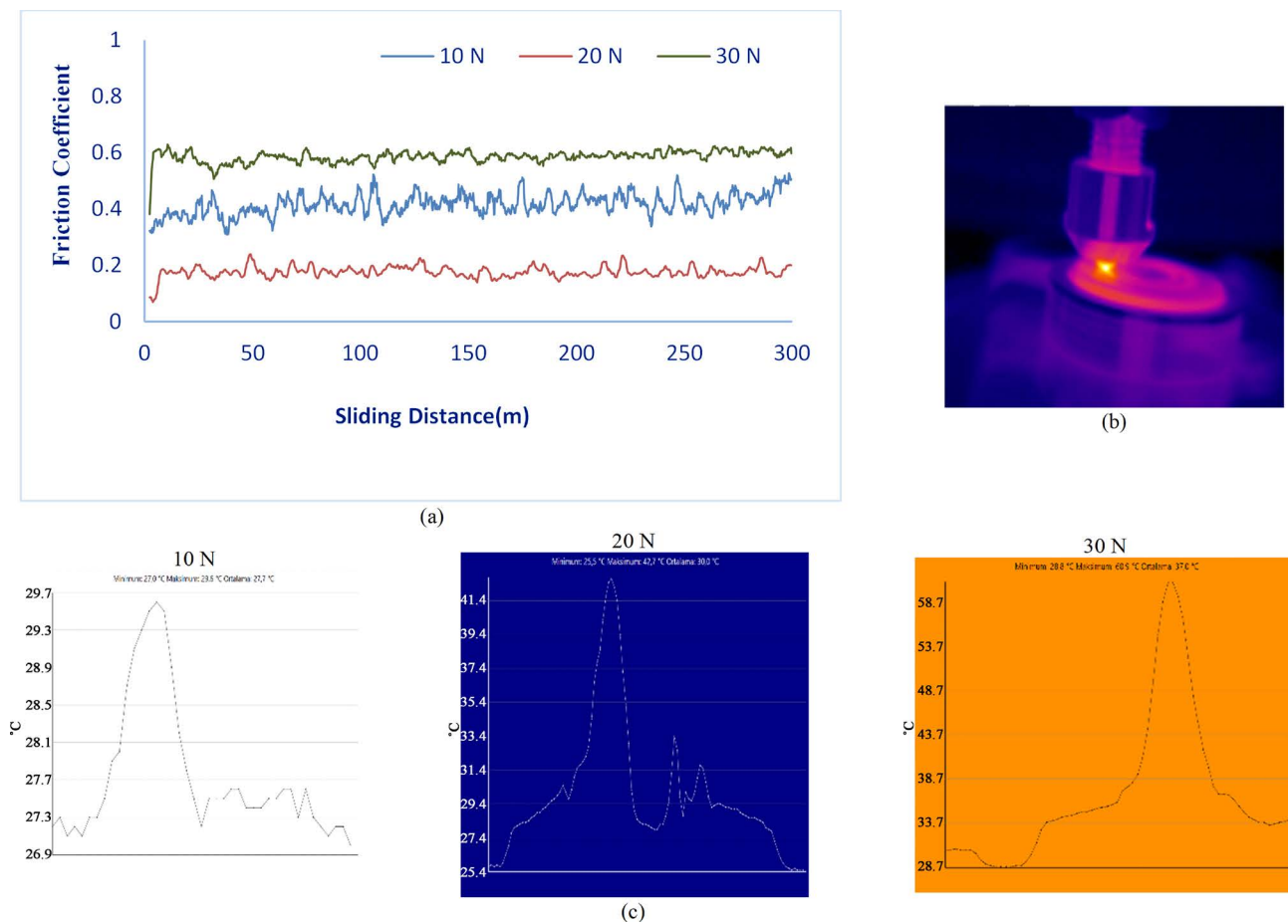


Figure 10. (a) The graph of friction coefficient-sliding distance between 10N - 30N; (b) The thermal visual taken with the thermal camera from the surface during the wear test; (c) the graph showing differences in surface temperature between 10N - 30N for the material S60.

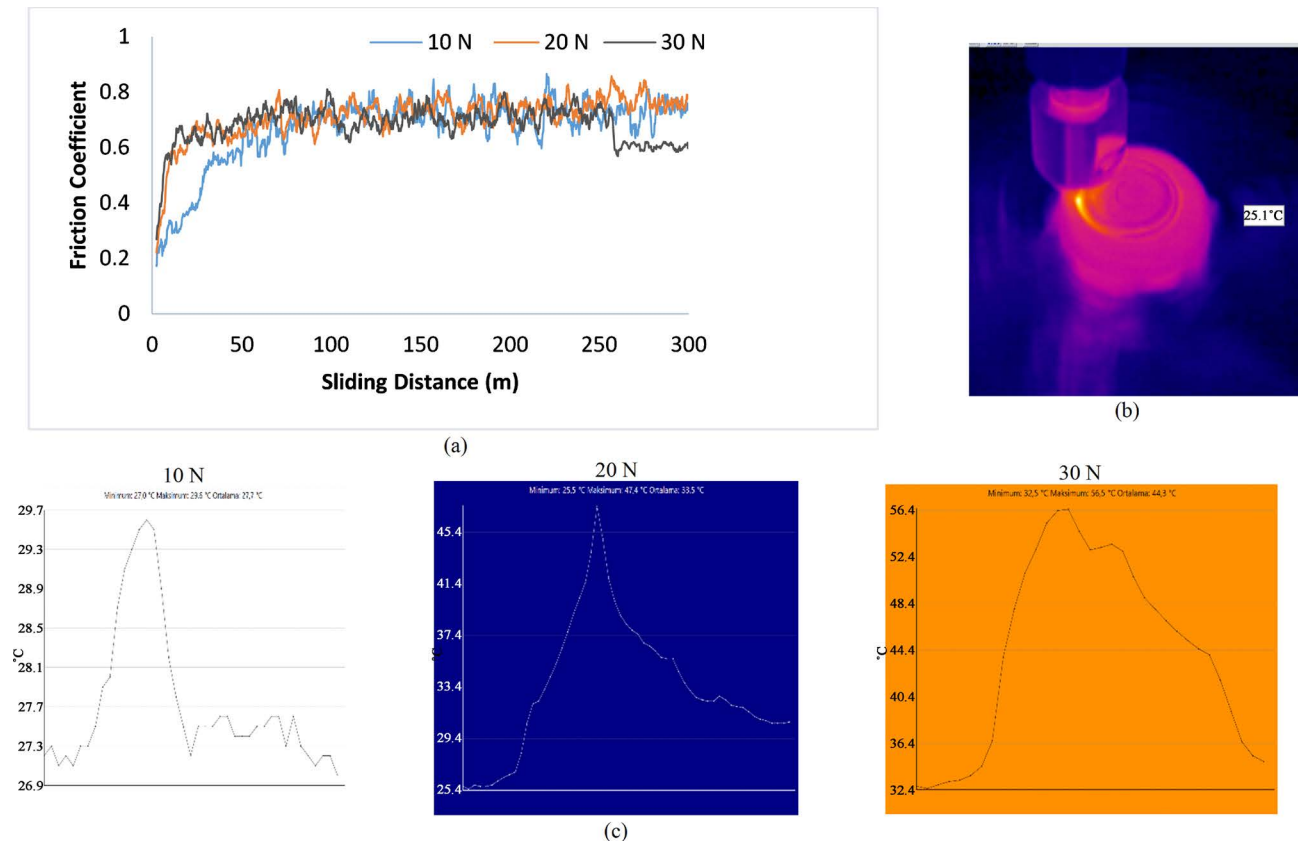


Figure 11. (a) The graph of friction coefficient-sliding distance between 10N - 30N; (b) The thermal visual taken with the thermal camera from the surface during the wear test; (c) the graph showing differences in surface temperature between 10N - 30N for the material S60B10.

first stage of the wear test, the peaks were unstable and the friction coefficient increased constantly with considerable peaks; additionally, inclinations seem to shift after the sliding distance of around 30 m (Figure 11(a)). The friction coefficients of S60B10 displayed similar patterns under all the weights used in the experiment (Figure 11(a)). Furthermore, there were also slight decreases in friction coefficients as the loads increased. The friction coefficient decreases significantly only during the wear test conducted under the load of 30N after the sliding distance of 250 m (Figure 11(a)). During wear, the temperature measurements for the material S60B10 recorded for every 50 m of the surface revealed that under the load of 10N, the temperature increased rapidly from the sliding distance of 50 m until around 150 m, then it dropped until 200 m (Figure 11(c)). Between the distances of 200 m and 300 m for 10N, the temperature fluctuated in the lower threshold (Figure 11(c)). For 20N and 30N, S60B10 displayed similar changes in temperature; it was recorded that the temperature increased rapidly until the distance of 150 m before dropping at the same rate between the distances of 200 m and 250 m and stabilising afterwards (Figure 11(c)).

Figures 12(a)-(c) shows the wear test results for the material containing wt20% B₄C (S55B20). The friction coefficient-sliding distance graph given in Figure 12(a)

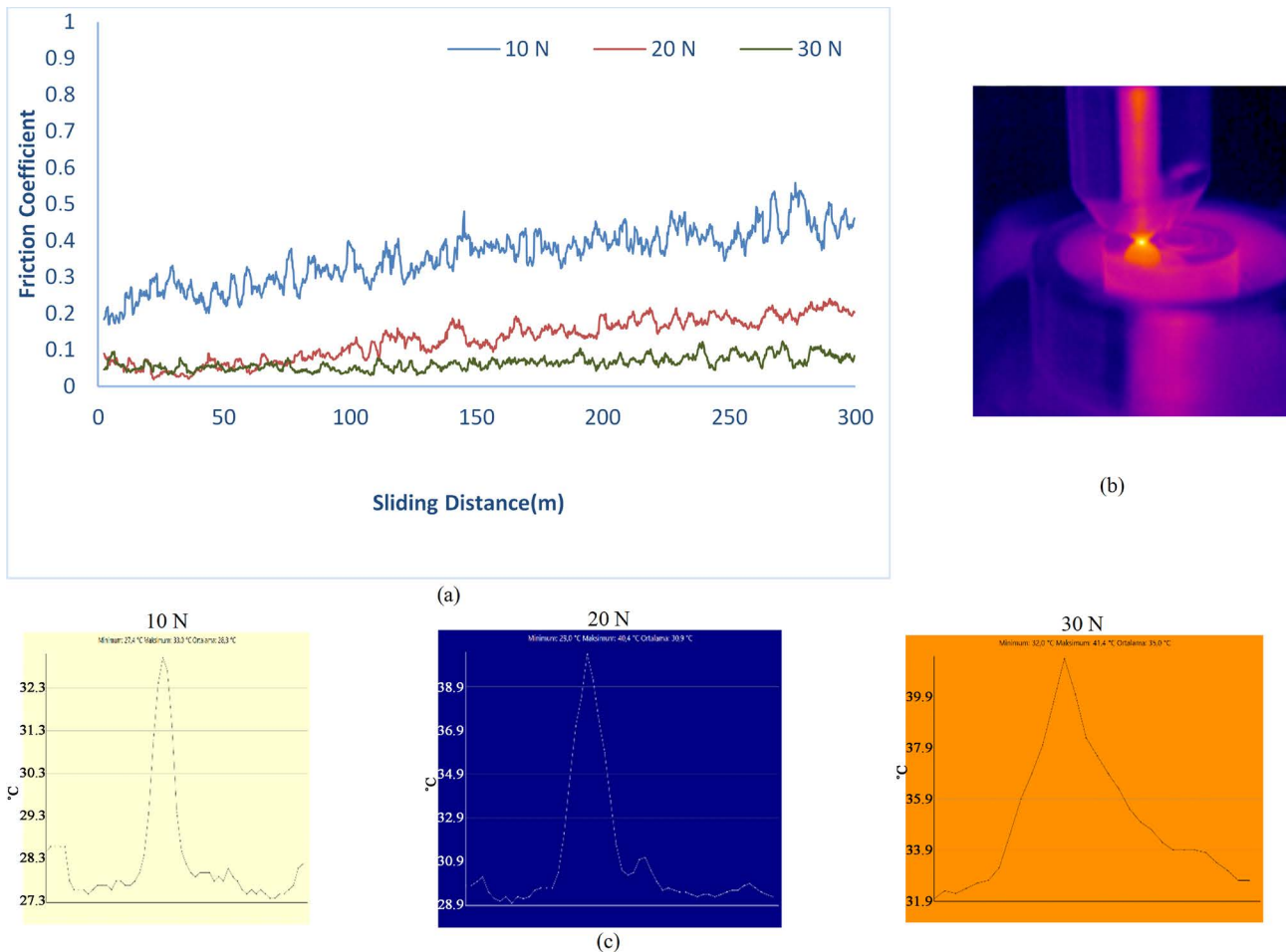


Figure 12. (a) The graph of friction coefficient-sliding distance between 10N - 30N; (b) The thermal visual taken with the thermal camera from the surface during the wear test; (c) the graph showing differences in surface temperature between 10N - 30N for the material S55B20.

reveals that under all the weights (10N - 30N), the friction coefficients of S55B20 increased constantly until the sliding distance of 300 m. At the same time, however, the friction coefficient decreased significantly as the load increased. Furthermore, fluctuations in the friction coefficients were prevalent throughout the sliding distance of 300 m for all the loads (**Figure 12(a)**). The temperature differences presented in **Figure 12(c)** shows that particularly for the weights of 10N and 20N, similar peaks occurred and the temperature rose and decreased sharply between the distances of 100 m and 200 m. For the load of 30N, the peak width increased and stabilised after around the distance of 250 m (**Figure 12(c)**).

The results of the pin-on-disc wear tests for S45B30 under the loads ranging between 10N and 30N indicated an increase in the friction coefficient under 10N and 20N (**Figure 13(a)**). As for the load of 30N, the friction coefficient values steadily increasing until 240 m of distance dropped after this point (**Figure 13(a)**). The friction coefficient values under the load of 20N were lower when compared with the values for the load of 10N (**Figure 13(a)**). Under the load of 30N and throughout the sliding distance of 300 m, the friction coefficient-sliding distance

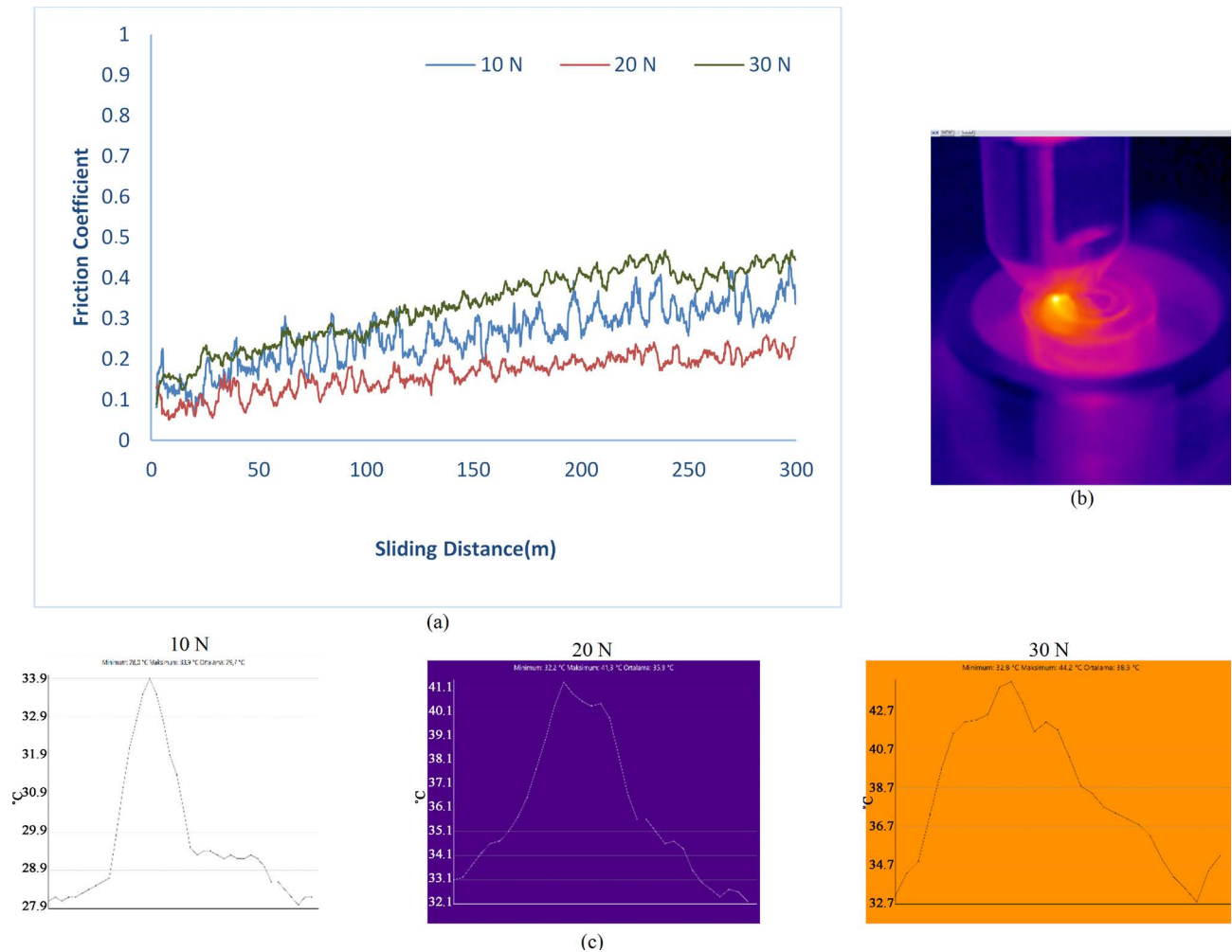


Figure 13. (a) The graph of friction coefficient-sliding distance between 10N - 30N; (b) The thermal visual taken with the thermal camera from the surface during the wear test; (c) the graph showing differences in surface temperature between 10N - 30N for the material S45B30.

graph given in **Figure 13(a)** shows higher friction coefficient values when compared with the other loads. Furthermore, during friction, the temperature values recorded for every 50 m of distance revealed that the temperature increases for approximately every 100 m of sliding distance under all loads (**Figure 13(c)**). On the other hand, the wear test conducted under 20N and 30N displayed similar changes in temperature with broad peak distributions (**Figure 13(c)**).

The outcomes of the pin-on-disc wear test conducted on the 1010 steel added into the epoxy and hardener mixture showed that the material S100E20 produces friction coefficient peaks ranging between the values of 0.2 and 0.5 (**Figure 14(a)**). When the abrasive load was increased to 20N, the friction coefficient values were seen to decline (**Figure 14(a)**). Then, when the load was further increased to 30N, the friction coefficient peaks decreased until the sliding distance of 70 m before increasing until the distance of 300 m (**Figure 14(a)**). However, S100E20 produced lower values for 30N when compared with the load of 10N (**Figure 14(a)**). The median temperature values recorded on the surface for the

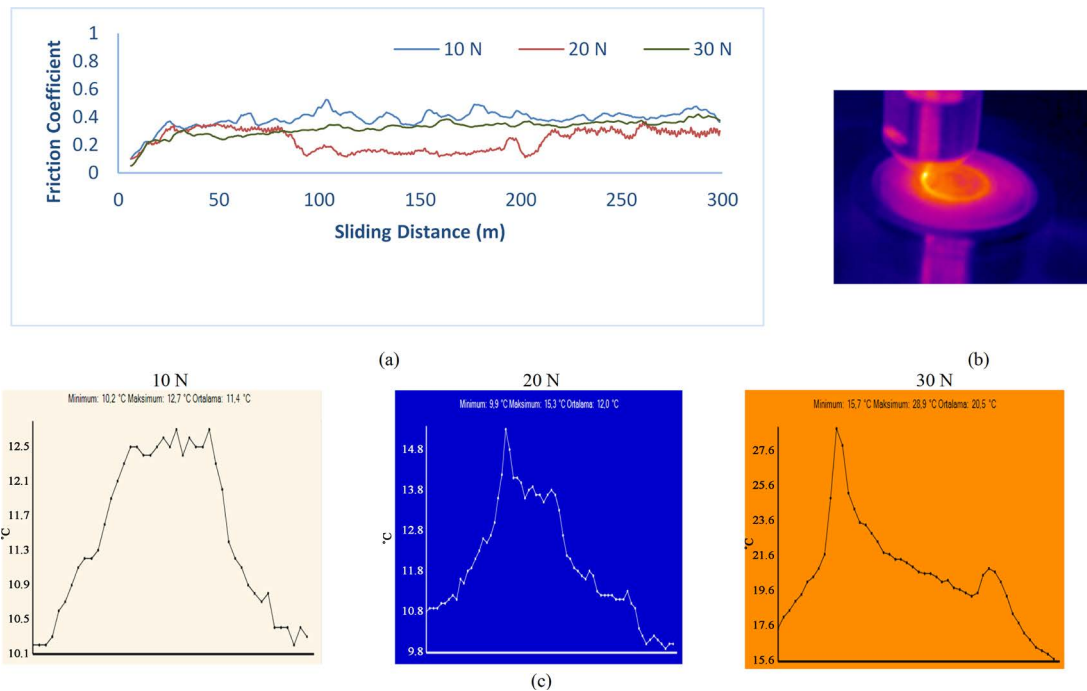


Figure 14. (a) The graph of friction coefficient-sliding distance between 10N - 30N; (b) The thermal visual taken with the thermal camera from the surface during the wear test; (c) the graph showing differences in surface temperature between 10N - 30N for the material S100E20.

loads ranging between 10N and 30N during wearing were measured to be 11.4°C for 10N, 12°C for 20N, and 20.5°C for 30N (Figure 14(c)).

Figures 15(a)-(c) shows the pin-on-disc wear tests for the material S60E20, prepared only through mixing without hot pressing and not subjected to any kind of hot processing. For all the loads, S60E20 displayed fluctuating friction peaks and similar patterns for the friction coefficient (Figure 15(a)). Once again, for all the loads (10N - 30N), the friction coefficient increased rapidly until the sliding distance of around 50 m (Figure 15(a)). After this distance, friction coefficient peaks were fluctuating within a stable range (Figure 15(a)). When the load was increased to 20N, the temperature increase saw a rise along with the friction coefficient values on the wear surface (Figure 15(a), Figure 15(c)). For 30N, the friction coefficient peaks were higher than those for 10N yet lower than those for 20N (Figure 15(a)). Upon examining the temperature changes on the surface during the wear test under the loads ranging between 10N and 30N, one can observe similar results, with the temperature reaching the maximum particularly between the distances of 200 m and 250 m, with the peak width increases as the load increases, as seen in Figure 15(c). The highest temperature peak width was observed during the wear test conducted under the load of 30N (Figure 15(c)).

Figures 16(a)-(c) shows the pin-on-disc wear tests for the material prepared to be added into epoxy and containing wt10% B₄C under the loads ranging between 10N and 30N. For all the loads, the material S60B10E20 produced high and unstably fluctuating friction peaks (Figure 16(a)). The first stage of the friction

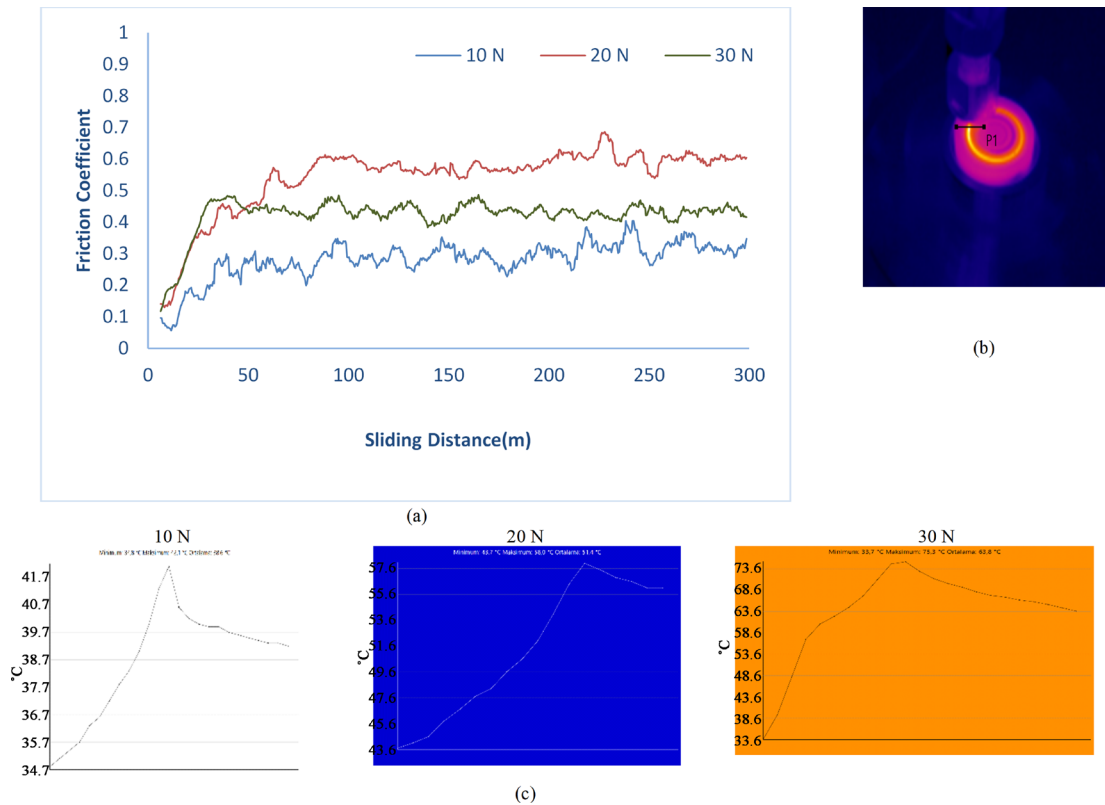


Figure 15. (a) The graph of friction coefficient-sliding distance between 10N - 30N; (b) The thermal visual taken with the thermal camera from the surface during the wear test; (c) the graph showing differences in surface temperature between 10N - 30N for the material S60E20.

and wear test conducted under loads ranging between 10N and 30N displayed unstable friction peaks and at the same stage, the friction coefficient increased constantly with considerable fluctuations (Figure 16(a)). Then, the friction peaks remained unstable while the changes in the friction coefficient fluctuations persisted within a lower range. Furthermore, when the load was increased to 20N, the friction coefficient dropped whereas they increased for the load of 30N despite displaying lower friction coefficient fluctuations and peaks, as seen in Figure 16(a). The temperature measurements made using thermal cameras during wearing on the surface showed that the temperatures reached the maximum value until the sliding distance of 200 - 250 m before declining (Figure 16(c)).

Figures 17(a)-(c) shows the pin-on-disc wear test results for the material S55B20E20, produced by adding the mixture containing wt55% 1010 steel and wt20% B₄C into the epoxy mixture, under the weights ranging between 10N and 30N. The analysis revealed peak values ranging between 0.4 and 0.6 for S55B20E20 under the weights ranging between 10N and 30N (Figure 17(a)). Furthermore, while the peak values were close for 10N and 20N, the friction coefficient values dropped for the load of 30N (Figure 17(a)). The peak intensities ranged between around 0.2 and 0.35 for S55B20E20 under 30N. The mean surface temperature values during wearing were recorded as 22.3°C, 22.9°C, and

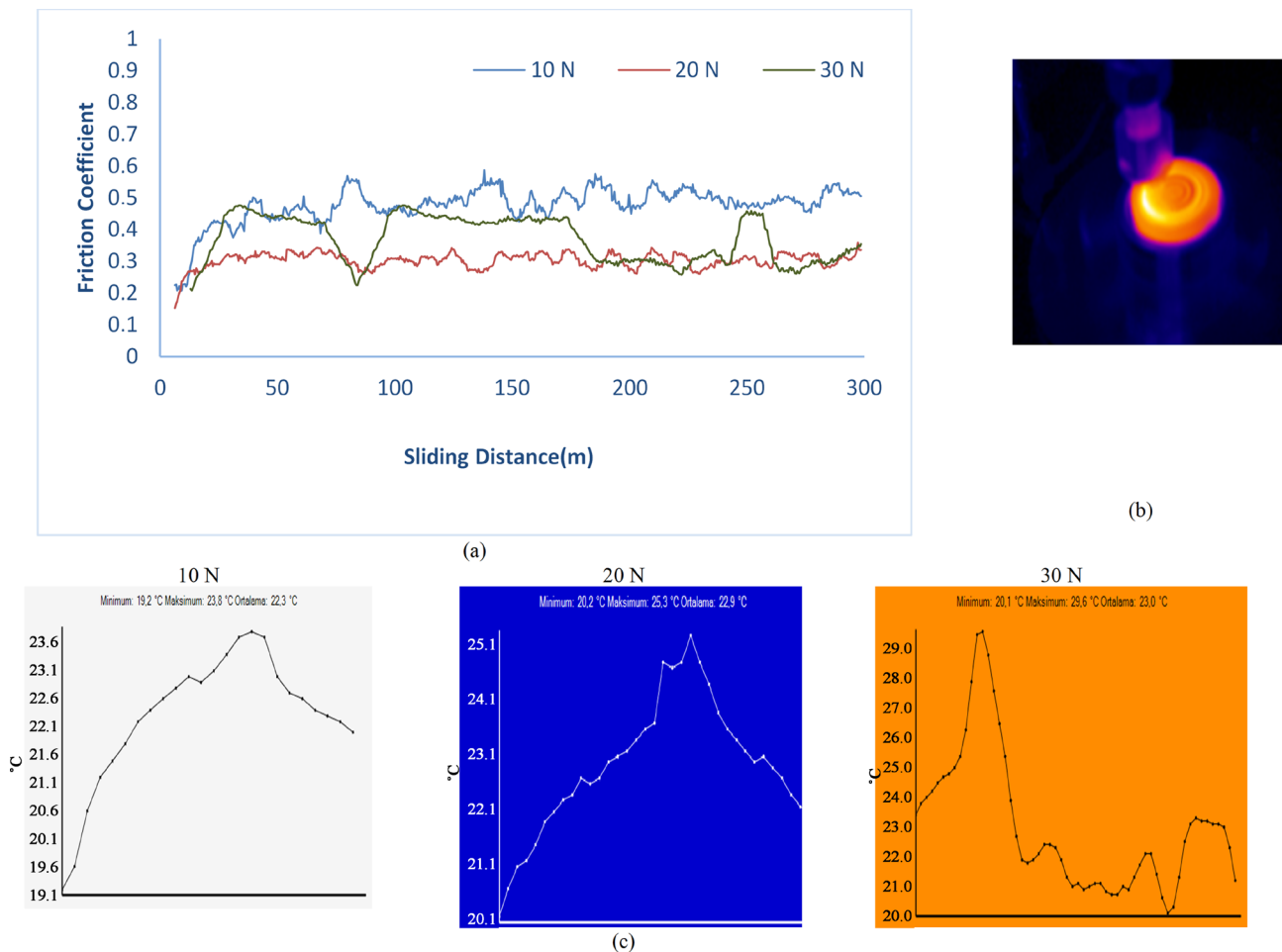


Figure 16. (a) The graph of friction coefficient-sliding distance between 10N - 30N; (b) The thermal visual taken with the thermal camera from the surface during the wear test; (c) the graph showing differences in surface temperature between 10N - 30N for the material S60B10E20.

23 °C for 10N, 20N, and 30N, respectively, as shown in **Figure 17(c)**.

Figures 18(a)-(c) shows the pin-on-disc wear test results for the material S45B30E20, prepared by adding the mixture of 1010 steel, SiC, MgO, H₃BO₃, and wt30% B₄C into the epoxy mixture, under 10N, 20N, and 30N. The wear test produced close results under all the loads for S45B30E20 until a distance of around 100 m (**Figure 18(a)**). After around 100 m, while the peaks remained close for 10N and 30N, they were higher for 20N (**Figure 18(a)**). The mean temperatures during wearing were recorded as 32.3 °C, 37.6 °C, and 46.8 °C for 10N, 20N, and 30N, respectively (**Figure 18(c)**). Therefore, it was observed that surface temperature increased as the load increased (**Figure 18(c)**).

4. Discussion

The materials S100 and S60, for which XRD results are given in **Figure 3(a)** & **Figure 3(b)**, are clearly seen to contain 1010 steel matrix and reinforcement compounds. Both materials contain the compound Fe₃C due to the 1010 steel content. Furthermore, unlike S100, S60 was also observed to contain the compounds

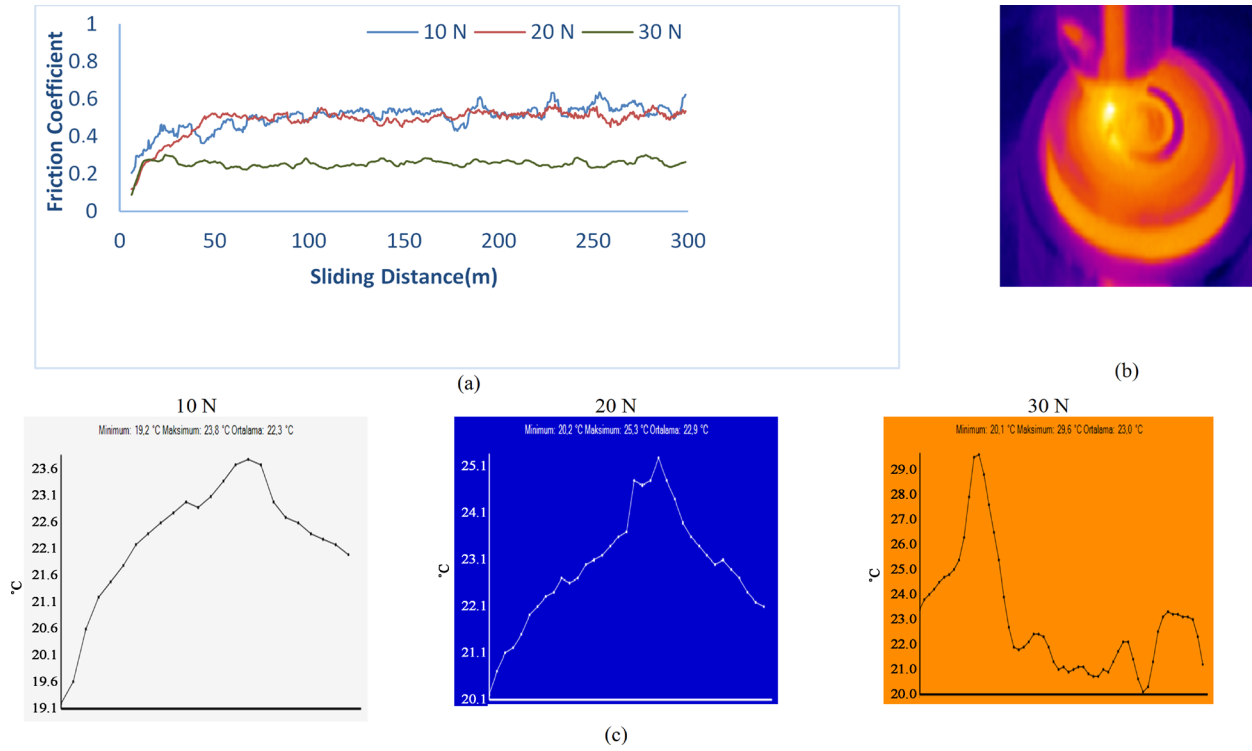


Figure 17. (a) The graph of friction coefficient-sliding distance between 10N - 30N; (b) The thermal visual taken with the thermal camera from the surface during the wear test; (c) the graph showing differences in surface temperature between 10N - 30N for the material S55B20E20.

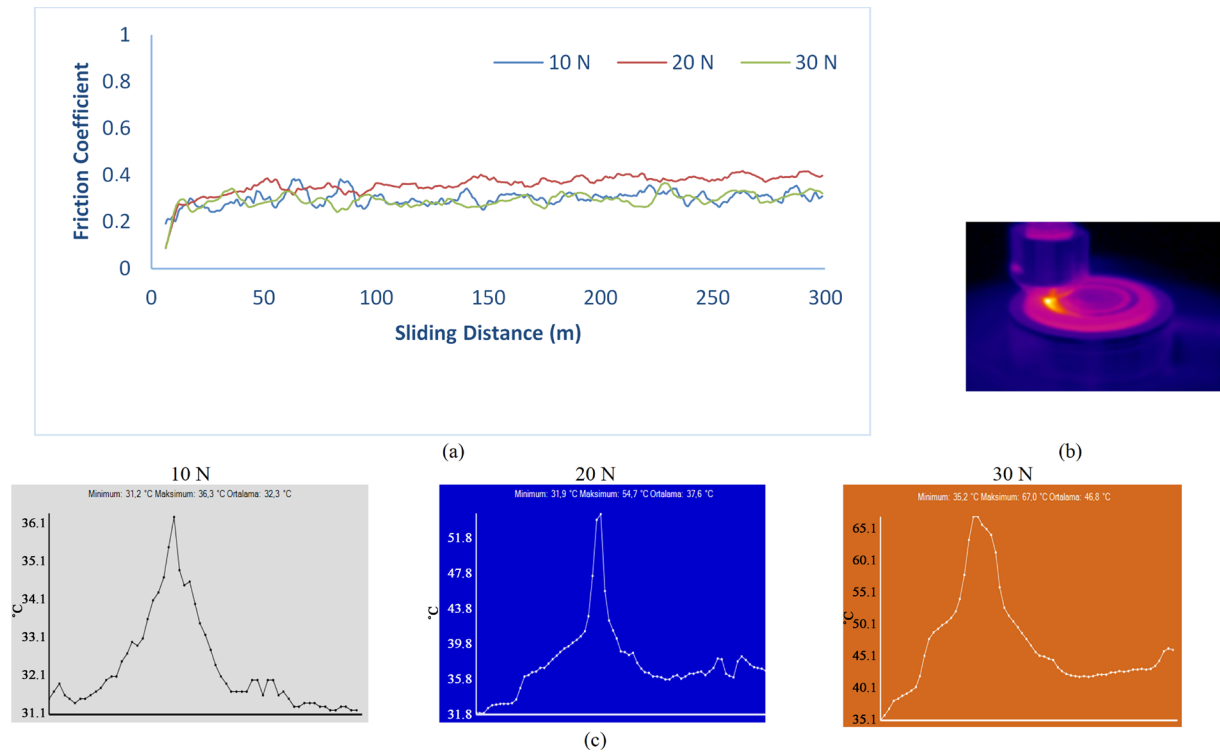


Figure 18. (a) The graph of friction coefficient-sliding distance between 10N - 30N; (b) The thermal visual taken with the thermal camera from the surface during the wear test; (c) the graph showing differences in surface temperature between 10N - 30N for the material S45B30E20.

SiC and H_3BO_3 , as seen in **Figure 3(a)** & **Figure 3(b)**. Upon examining the peak intensities of S100 and S60, the peak intensity for the latter was found to decrease significantly due to its structure consisting of SiC, MgO ve H_3BO_3 (**Figure 3(a)** & **Figure 3(b)**). The peak intensity varying between 0 and 140 for S100 decreased to the range of 0-60 for S60 (**Figure 3(a)** & **Figure 3(b)**). **Figures 4(a)-(c)** show XRD analysis results for the materials S60B10, S55B20, and S45B30. Based on these results, **Figures 4(a)-(c)** also show that all these materials contain the phase structures of Fe_2O_3 , SiC, MgO, H_3BO_3 , and B_4C in addition to Fe_3C . SiC and B_4C are crystallographic phases [20]. Therefore, B_4C added in varying amounts affected the crystallography of the materials. This means that while all the phases showed clear and distinct peak distributions in the XRD results for S60B10 and S55B20, the peak distribution rates dropped for S45B30. However, peak intensity rose as the B_4C amount increased and S45B30 containing 30% B_4C displayed the highest peak intensity among the materials containing B_4C (**Figures 4(a)-(c)**). Furthermore, the phase H_3BO_3 widely and clearly seen in the range of $2\theta = 10 - 30$ for S60B10 and S55B20 were not observed in the XRD graph for the material S45B30. The XRD peaks generally displayed non-high peak intensities for SiC and B_4C (**Figure 3(b)**, **Figures 4(a)-(c)**). These were found to be in line with other studies in the literature and the peaks for SiC and B_4C were less distinct [21] [22] [23] [24].

The SEM visuals of S60 and S55B20 show that both materials have main structures with indefinite grain boundaries due to liquid phase sintering (**Figure 2(a)**, **Figure 3(a)**). **Figure 2(a)** & **Figure 2(b)** and **Figure 3(a)** & **Figure 3(b)** shows that both materials also form dark grey phases structures containing Si and C on different heights containing Mg, C, and O. However, it was observed from the SEM visual for S60 that phases containing Mg, O, and C are larger in size when compared to S55B20 and that these phase structures are more frequent with varying sizes (**Figure 2(a)**, **Figure 3(a)**). **Figure 2(a)** and **Figure 3(a)** show that structures containing Si and C are fewer in S55B20 when compared to S60. The sliding of ceramics subjected to wear in ambient conditions arises from oxide structures on the material surface [20]. This means that sliding on ceramics occur due to oxide structures on their surface [20]. The study argues that the reason why sliding occurs on S60 and S55B20 during wear is the surface oxide structures observed during EDS analyses. Unlike S60 and S55B20, the SEM visual for S60E20 and S55B20E20 containing wt20% reveals that the materials, in addition to having a flat main matrix, contain shallow surface holes and white spherical structures (**Figure 4(a)**, **Figure 5(a)**). However, **Figure 5(a)** shows that for the material S55B20E20 produced by adding B_4C to S60E20, the number and depth of the surface holes are lower when compared to S60E20 while the amount of white spherical structures increases and their sizes decrease slightly. The EDS analysis results for the materials S60E20 and S55B20E20 revealed that while the materials contain phases consisting of Fe, Si, Mg, B, C, and O, the white spheres on the surface contain Fe, Si, C, and O (**Figure 4(a)**, **Figure 5(a)**).

A pin-on-disc wear test was conducted on all the materials under a speed of 300 rpm, with loads ranging between 10N and 30N, and with a sliding distance of 300 m. Furthermore, thermal cameras were used to measure the temperatures on the surface for every 50 m of sliding distance in order to examine the impacts of temperature. For all the materials, the first stage of the friction and wear test conducted under loads ranging between 10N and 30N was unstable and, during this stage, the friction coefficients increased constantly and rapidly with significant fluctuations. Dependent on these factors, the friction coefficient-sliding distance graph for S100 indicated fluctuating friction peaks and similar patterns for all the loads (10N - 30N) (**Figure 9(a)**). Following the first stage, after a sliding distance of around 20 m, the friction peaks were more stable, and the friction coefficient peaks ranged between 0.6 and 0.8. However, the friction peaks were fluctuating for all the loads used during the experiment (**Figure 9(a)**). For S100, the friction coefficient values dropped visibly, particularly after the sliding distance of 100 m as the load increased. Furthermore, **Figure 9(c)** shows the rapid increase in the surface temperature for S100 under all the loads, particularly after the sliding distance of 100 m. During the pin-on-disc wear test conducted under 10N, the surface temperature measured between the wear balls and the interface was 32.3°C while it rose to 37.4°C under 20N and 48.5°C under 30N (**Figure 9(c)**). For S60, the difference between the friction coefficient peaks obtained under varying loads was evident, ranging between 0.2 and 0.4 for 10N, between 0.1 and 0.2 for 20N, and around 0.6 for 30N (**Figure 10(a)**). This means that while the friction coefficient drops significantly under the wear load of 20N for S60, the load of 30N results in a dramatic increase, leading to the maximum value for the material (**Figure 10(a)**). The mean surface temperatures during the wear test were recorded as 27.7°C for 10N, 30°C for 20N, and 37°C for 30N (**Figure 10(c)**). The peak intensities were close for the material S60B10 while carrying loads ranging between 10N and 30N (**Figure 11(a)**). Only S60B10 displayed significant decreases in terms of friction coefficient after the sliding distance of around 250 m, ranging between 0.5 and 0.8 (**Figure 11(a)**). After the sliding distance of 300 m, the mean surface temperatures on S60B10 were recorded as 27.7°C for 10N, 33.5°C for 20N, and 35°C for 30N (**Figure 11(c)**). For S55B20, the pin-on-disc wear test conducted under loads ranging from 10N to 30N showed that the friction coefficient decreased evidently as the load increased. To be more precise, the friction coefficient ranged between 0.2 and 0.4 for 10N and between 0.1 and 0.2 for 20N; the value fell below 0.1 under 30N, as shown in **Figure 12(a)**. The mean surface temperatures rose in direct proportion to load, being recorded as 28.3°C for 10N, 30.9°C for 20N, and 35°C for 30N (**Figure 12(c)**). S45B20 displayed lower frictional force values with ranging between 0.1 and 0.3 for 10N and between 0.1 and 0.2 for 20N; this decrease was reversed under the load of 30N with friction coefficient values ranging between 0.2 and 0.4 (**Figure 13(a)**). The mean surface temperatures increased proportionately to the amount of load on the material, being recorded as 29.7°C for 10N, 35.9°C for 20N, and 38.3°C

for 30N (**Figure 13(c)**).

The study also examines the impacts of adding a mixture of 1010 steel, SiC, MgO, and B₄C into epoxy on the wear resistance of the latter. The results of the pin-on-disc wear test conducted on these materials showed that the friction coefficient of S60E20 shows apparent differences for loads ranging from 10N to 30N. For S60E20, the highest friction coefficient value was observed under 20N (around 0.5 - 0.6) while the lowest value was recorded under 10N (around 0.2 - 0.35) (**Figure 15(a)**). Under the load of 30N, the friction coefficient value was found to range between around 0.35 and 0.5, which is an average value when compared to the results obtained under different loads (**Figure 15(a)**). In other words, while the friction coefficient rose upon increasing the load to 20N, the peak intensity for the friction coefficient dropped under the load of 30N (**Figure 15(a)**). However, the tests under 10N did not result in higher friction coefficient peak intensities (**Figure 15(a)**). Therefore, increasing the load applied during the wear test also increases the contact surface. The increase in the contact surface also gives rise to interface temperatures [25]. The mean surface temperatures for S60E20 recorded during the wear test were 58.6°C for 10N, 51.4°C for 20N, and 63.8°C for 30N (**Figure 15(c)**). In other words, the mean temperature values recorded between the alumina ball and the surface of the material S60E20 rose as the load increased (**Figure 15(c)**). For the material S60B10E20 containing wt10% B₄C, the friction coefficient fell significantly as the load was increased to 20N. The value increased in comparison to 20N after increasing the load to 30N, displaying unstable friction coefficient peaks (**Figure 16(a)**). However, these results were lower when compared to the results of the wear test conducted under the load of 10N (**Figure 16(a)**). The mean temperature values recorded at the interface between the alumina wear ball and the contact point on S60B10E20 were 22.3°C for 10N, 22.9°C for 20N, and 23°C for 30N (**Figure 16(c)**). Under 10N, deformation and delamination wear mechanism occurs at the sliding distances of 100 m and 300 m [26]. Delamination wear mechanism arises as a result of the material being separated from the surface due to wearing because fractures occur on the delaminated spot [26]. Work hardening emerging at this stage leads to the deformation of the matrix [24]. Work hardening rises as the wear load increases, leading to fractures on the matrix and reinforcement interface [24]. It causes delamination wear on the fractures [24]. Furthermore, the occurrence of work hardening contributes to the better performance of the material in terms of wear resistance [27] [28].

The wear tests results indicated significant decreases in friction coefficients for the material S60 produced by adding SiC, MgO, and H₃BO₃ into 1010 steel (**Figure 9(a)**, **Figure 10(a)**). Consequently, these additional materials were found to enhance the wear resistance of 1010 steel. The friction coefficient was decreased by adding B₄C to the material S60. Among the additions of B₄C into the materials, the material S55B20 containing wt20% B₄C displayed the best results (**Figure 11(a)**-**Figure 13(a)**). In this respect, S55B20 had the highest wear resistance

(**Figure 12(a)**). The review of the existing literature revealed that friction coefficient values decline as the amount of SiC and B₄C added to the material increases [24]. It also reacts with the environment as B₄C breaks during wearing [24]. A layer of B₂O₃ is formed on the surface as a result of this reaction [24]. Therefore, the oxide layer of B₂O₃ was directly associated with the friction coefficient [24]. The oxide layer on the surface acts as a lubricant, decreasing the friction coefficient [29] [30] [31]. The surface temperature measurements made during the wear test revealed that the mean surface temperature for the material S60 produced by adding SiC, MgO, and H₃BO₃ into 1010 steel was much lower when compared to S100 (**Figure 9(c)**-**Figure 10(c)**). The addition of B₄C resulted in a decrease in the surface temperature, particularly during the wear test of the material S55B20 containing wt20% B₄C (**Figure 11(c)**). This is one of the primary reasons behind the significant decrease in friction coefficients for materials with additional B₄C, particularly S55B20.

In the second group of materials produced by adding the mixture of the aforementioned compounds into the epoxy mixture, similar results were observed and the compounds of SiC, MgO, and H₃BO₃ decreased the friction coefficient for the epoxy material containing 1010 steel (S100E20). Therefore, S60E20 displayed lower friction coefficient peaks when compared to S100E20 (**Figure 14(a)**, **Figure 15(a)**). Similarly, the addition of B₄C contributed to a further decrease in friction coefficients. The mean surface temperatures recorded during the wear test revealed the contribution of B₄C to the decrease in surface temperatures. As a result of these factors, the decrease in friction coefficients and surface temperatures along with the addition of SiC, MgO, H₃BO₃, and B₄C enhanced wear resistance.

5. Conclusion

- The XRD results for S100 and S60 revealed that both materials consist of Fe₃C in addition to the latter containing the phases of SiC and H₃BO₃. The addition of SiC, MgO, and H₃BO₃ into 1010 steel to obtain S60 significantly decreases peak intensity. One might argue that the decrease in peak intensity leads to a decrease in crystallography.
- The XRD results for materials to which varying amounts of B₄C were added showed that B₄C affects crystallography, causing an increase in peak intensity. Furthermore, all the phase structures in these materials (S60B10, S55B20, and S45B30) were found to display clear and distinct peak distributions.
- The analysis of the SEM-EDS visuals obtained from the surfaces of S60 and S55B20 revealed that the main structures have indefinite grain boundaries due to liquid phase sintering and contain structures containing Mg, C, O, Si, and C. Furthermore, the sizes of the structures containing Mg, C, and O shrunk with the addition of B₄C. Their numbers on the surface analysed with SEM increased while the formation of the structure containing Si and C declined.
- The SEM visual obtained from the materials S60E20 and S55B20E20 indicated

flat main matrices and surfaces with non-deep superficial holes due to hardening (drying) and white spherical structures. Additionally, the number and depth of the holes on the surface of S55B20 were lower when compared to S60E20; the white spherical structures were more abundant in number despite being slightly smaller in the former.

- The pin-on-disc wear tests revealed that the friction coefficient values were decreased by adding SiC, MgO, and H₃BO₃ into 1010 steel. The friction coefficients were further decreased with the addition of B₄C. However, the lowest friction coefficient value was recorded for the material S55B20 containing wt20% B₄C. Consequently, S55B20 had the highest score in terms of wear resistance.
- The assessment of the materials S100E20 and S60E20 prepared by mixing into epoxy revealed that the latter had lower friction coefficients, with the materials containing B₄C displaying even lower values. The lowest friction coefficient among the materials containing B₄C was observed for the material S60B20E20 containing wt20% B₄C. Consequently, S60B20E20 had the highest score in terms of wear resistance.
- A part of the components break away from the materials during wearing stuck onto the surface, acting as a lubricant. This lubricating effect culminated in both lower surface temperatures and friction coefficients. Therefore, in many materials, the lubricating impact was more apparent as the number of components break away from the material increased, resulting in a decrease in mean surface temperatures and friction coefficients.

Conflicts of Interest

The authors declare no conflicts of interest regarding the publication of this paper.

References

- [1] Hudson, C.M. and Rich T.P. (Eds.) (1986) Case Histories Involving Fatigue and Fracture Mechanics: A Symposium. No. 918, ASTM International, West Conshohocken. <https://doi.org/10.1520/STP918-EB>
- [2] Elayaperumal, K. and Raja, V.S. (2015) Corrosion Failures: Theory, Case Studies, and Solutions. John Wiley & Sons, Hoboken. <https://doi.org/10.1002/9781119043270>
- [3] Gagg, C.R. and Lewis, P.R. (2007) Wear as a Product Failure Mechanism—Overview and Case Studies. *Engineering Failure Analysis*, **14**, 1618-1640. <https://doi.org/10.1016/j.engfailanal.2006.11.064>
- [4] Bhadeshia, H. and Honeycombe, R. (2017) Steels: Microstructure and Properties. Butterworth-Heinemann, Oxford.
- [5] Davis, J.R. (Ed.) (1994) Stainless Steels. ASM International, West Conshohocken.
- [6] Santana, D.A., Koga, G.Y., Wolf, W., Bataev, I.A., Ruktuev, A.A., Bolfarini, C., *et al.* (2020) Wear-Resistant Boride Reinforced Steel Coatings Produced by Non-Vacuum Electron Beam Cladding. *Surface and Coatings Technology*, **386**, Article ID: 125466. <https://doi.org/10.1016/j.surfcoat.2020.125466>

- [7] Monson, P.J.E. and Steen, W.M. (1990) Comparison of Laser Hardfacing with Conventional Processes. *Surface Engineering*, **6**, 185-193. <https://doi.org/10.1179/sur.1990.6.3.185>
- [8] Bulloch, J.H. and Henderson, J.L. (1991) Some Considerations of Wear and Hardfacing Materials. *International Journal of Pressure Vessels and Piping*, **46**, 251-267. [https://doi.org/10.1016/0308-0161\(91\)90073-B](https://doi.org/10.1016/0308-0161(91)90073-B)
- [9] Mellor, B.G. (2006) Welding Surface Treatment Methods for Protection against Wear. In: Mellor, B.G., Ed., *Surface Coatings for Protection against Wear*, Woodhead Publishing, Cambridge, 302-376. https://doi.org/10.1533/9781845691561_302
- [10] Ahn, D.G. (2013) Hardfacing Technologies for Improvement of Wear Characteristics of Hot Working Tools: A Review. *International Journal of Precision Engineering and Manufacturing*, **14**, 1271-1283. <https://doi.org/10.1007/s12541-013-0174-z>
- [11] Iakovou, R., Bourithis, L. and Papadimitriou, G. (2002) Synthesis of Boride Coatings on Steel Using Plasma Transferred Arc (PTA) Process and Its Wear Performance. *Wear*, **252**, 1007-1015. [https://doi.org/10.1016/S0043-1648\(02\)00056-X](https://doi.org/10.1016/S0043-1648(02)00056-X)
- [12] Darabara, M., Papadimitriou, G.D. and Bourithis, L. (2006) Production of Fe-B-TiB₂ Metal Matrix Composites on Steel Surface. *Surface and Coatings Technology*, **201**, 3518-3523. <https://doi.org/10.1016/j.surfcoat.2006.08.105>
- [13] Eyre, T.S. (1975) Effect of Boronising on Friction and Wear of Ferrous Metals. *Wear*, **34**, 383-397. [https://doi.org/10.1016/0043-1648\(75\)90105-2](https://doi.org/10.1016/0043-1648(75)90105-2)
- [14] Rus, J., De Leal, C.L. and Tsipas, D.N. (1985) Boronizing of 304 Steel. *Journal of Materials Science Letters*, **4**, 558-560. <https://doi.org/10.1007/BF00720032>
- [15] Gopalakrishnan, P., Shankar, P., Subba Rao, R.V., Sundar, M. and Ramakrishnan, S.S. (2001) Laser Surface Modification of Low Carbon Borided Steels. *Scripta Materialia*, **44**, 707-712. [https://doi.org/10.1016/S1359-6462\(00\)00674-6](https://doi.org/10.1016/S1359-6462(00)00674-6)
- [16] Carrera-Espinoza, R., Figueroa-López, U., Martínez-Trinidad, J., Campos-Silva, I., Hernández-Sánchez, E. and Motallebzadeh, A. (2016) Tribological Behavior of Borided AISI 1018 Steel under Linear Reciprocating Sliding Conditions. *Wear*, **362**, 1-7. <https://doi.org/10.1016/j.wear.2016.05.003>
- [17] Sajed, M. and Seyedkashi, S. H. (2020) Solid-State Local Micro-Alloying of Thick st37 Steel Plates with SiC Powder Using a Modified Friction Hydro-Pillar Process. *Journal of Materials Research and Technology*, **9**, 7158-7171. <https://doi.org/10.1016/j.jmrt.2020.04.068>
- [18] Li, J., Zong, B.Y., Wang, Y.M. and Zhuang, W.B. (2010) Experiment and Modeling of Mechanical Properties on Iron Matrix Composites Reinforced by Different Types of Ceramic Particles. *Materials Science and Engineering: A*, **527**, 7545-7551. <https://doi.org/10.1016/j.msea.2010.08.029>
- [19] Wu, C.L., Zhang, S., Zhang, C.H., Zhang, J.B., Liu Y. and Chen J. (2019) Effects of SiC Content on Phase Evolution and Corrosion Behavior of SiC-Reinforced 316L Stainless Steel Matrix Composites by Laser Melting Deposition. *Optics & Laser Technology*, **115**, 134-139. <https://doi.org/10.1016/j.optlastec.2019.02.029>
- [20] Jamale, S. and Kumar, B.M. (2020) Sintering and Sliding Wear Studies of B₄C-SiC Composites. *International Journal of Refractory Metals and Hard Materials*, **87**, Article ID: 105124. <https://doi.org/10.1016/j.ijrmhm.2019.105124>
- [21] Yuvaraj, N. and Aravindan, S. (2015) Fabrication of Al5083/B₄C Surface Composite by Friction Stir Processing and Its Tribological Characterization. *Journal of Materials Research and Technology*, **4**, 398-410. <https://doi.org/10.1016/j.jmrt.2015.02.006>

- [22] Sambathkumar, M., Navaneethakrishnan, P., Ponappa, K.S.K.S. and Sasikumar, K.S.K. (2017) Mechanical and Corrosion Behavior of Al7075 (Hybrid) Metal Matrix Composites by Two Step Stir Casting Process. *Latin American Journal of Solids and Structures*, **14**, 243-255. <https://doi.org/10.1590/1679-78253132>
- [23] Monikandan, V.V., Joseph, M.A. and Rajendrakumar, P.K. (2016) Dry Sliding Wear Studies of Aluminum Matrix Hybrid Composites. *Resource-Efficient Technologies*, **2**, S12-S24. <https://doi.org/10.1016/j.refit.2016.10.002>
- [24] Halil, K., İsmail, O., Sibel, D. and Ramazan, Ç. (2019) Wear and Mechanical Properties of Al6061/SiC/B₄C Hybrid Composites Produced with Powder Metallurgy. *Journal of Materials Research and Technology*, **8**, 5348-5361. <https://doi.org/10.1016/j.jmrt.2019.09.002>
- [25] Gård, A., Hallbäck, N., Krakhmalev, P. and Bergström J. (2010) Temperature Effects on Adhesive Wear in Dry Sliding Contacts. *Wear*, **268**, 968-975. <https://doi.org/10.1016/j.wear.2009.12.007>
- [26] Wang, D.Z., Peng, H.X., Liu, J. and Yao, C.K. (1995) Wear Behaviour and Microstructural Changes of SiCw-Al Composite under Unlubricated Sliding Friction. *Wear*, **184**, 187-192. [https://doi.org/10.1016/0043-1648\(94\)06577-2](https://doi.org/10.1016/0043-1648(94)06577-2)
- [27] He, Z.M., Jiang, Q.C., Fu, S.B. and Xie, J.P. (1987) Improved Work-Hardening Ability and Wear Resistance of Austenitic Manganese Steel under Non-Severe Impact-Loading Conditions. *Wear*, **120**, 305-319. [https://doi.org/10.1016/0043-1648\(87\)90024-X](https://doi.org/10.1016/0043-1648(87)90024-X)
- [28] Jha, A.K., Prasad, B.K., Modi, O.P., Das, S. and Yegneswaran, A.H. (2003) Correlating Microstructural Features and Mechanical Properties with Abrasion Resistance of a High Strength Low Alloy Steel. *Wear*, **254**, 120-128. [https://doi.org/10.1016/S0043-1648\(02\)00309-5](https://doi.org/10.1016/S0043-1648(02)00309-5)
- [29] Vergne, C., Boher, C., Gras, R. and Levailant, C. (2006) Influence of Oxides on Friction in Hot Rolling: Experimental Investigations and Tribological Modelling. *Wear*, **260**, 957-975. <https://doi.org/10.1016/j.wear.2005.06.005>
- [30] Li, C.X. and Bell, T. (2004) Sliding Wear Properties of Active Screen Plasma Nitrided 316 Austenitic Stainless Steel. *Wear*, **256**, 1144-1152. <https://doi.org/10.1016/j.wear.2003.07.006>
- [31] Li, X.Y. and Tandon, K.N. (2000) Microstructural Characterization of Mechanically Mixed Layer and Wear Debris in Sliding Wear of an Al Alloy and an Al Based Composite. *Wear*, **245**, 148-161. [https://doi.org/10.1016/S0043-1648\(00\)00475-0](https://doi.org/10.1016/S0043-1648(00)00475-0)